On the design of porous structures with enhanced fatigue life

Farhad Javid [a], Jia Liu [a], Ahmad Rafsanjani [a], Megan Schaenzer [b], Minh Quan Pham [b], David Backman [c], Scott Yandt [c], Matthew C. Innes [b], Christopher Booth-Morrison [b], Miklos Gerendas [d], Thomas Scarinci [d], Ali Shanian [b], Katia Bertoldi [a,e,*]

[a] Harvard John A. Paulson School of Engineering and Applied Sciences, Harvard University, Cambridge, MA, 02138, USA
[b] Siemens Power and Gas, 9545 Cote de Liesse, Dorval, Québec, H9P 1A5, Canada
[c] Aerospace Portfolio, National Research Council Canada, 1200 Montreal Road, Building M3, Ottawa, Ontario, K1A 0R6, Canada
[d] Rolls-Royce Deutschland Ltd. & Co. KG, Dahlewitz, Blankenfelde-Mahlow, Germany
[e] Kavli Institute, Harvard University, Cambridge, MA, 02138, USA

ARTICLE INFO

ABSTRACT

Many components of gas turbines, including the combustion liners, ducts, casings and sealing structures, comprise metallic sheets perforated with arrays of circular cooling holes. These parts are highly prone to fatigue failure due to the stresses induced by temperature variations during operation. Here, we demonstrate both experimentally and numerically that the fatigue life of these porous components can be greatly enhanced by carefully designing the pores' shape. In particular, we show that while the fatigue life of a metallic sheet with a square array of conventional circular cooling holes is <100k cycles, by replacing the pores with novel orthogonal *S-shaped* holes the life of the structure increases up to more than one million cycles. This is because the S-shaped pores introduce a soft mode of deformation based on rotation of the domains between neighboring holes that significantly affect the stress distribution and crack propagation in the structure.

© 2017 Elsevier Ltd. All rights reserved.

Gas turbines are important, widespread, and reliable devices that fulfill a variety of power needs from driving tanks, jets and helicopters to power generation and industrial power uses [1]. Since they operate at temperatures that exceed the melting points of the materials typically used for their construction, a major challenge facing turbine components is the incorporation of a cooling functionality within the system. Film cooling has emerged as an efficient method to reduce component temperatures and is currently used in virtually all of today's aircraft turbine engines and in many power-generation turbine engines [2]. In film cooling, low-temperature air is fed through small circular holes to provide a film of cool air insulating the component from the hot combustion gases. While the film cooling functionality is necessary to maintain the material integrity of the hot section components, it also introduces stress concentration features which can drive fatigue crack growth and failure. Several studies have considered the shape optimization of cooling holes [3–6]. However, they have only focused on their cooling functionality and neglected their effect on the mechanical performance. Hence, there is a need to identify cooling features resulting in enhanced fatigue life while still providing the necessary cooling functionality.

Here, we combine experiments and simulations to demonstrate that the fatigue life of metallic periodic porous sheets can be greatly enhanced by carefully designing the shape of the holes. Particularly, we show that, while a metallic sheet with a square array of conventional circular cooling holes fails before 100k cycles, by replacing the pores with mutually orthogonal S-shaped holes the structure is capable of carrying load upon one million cycles. We study the mechanism resulting in this remarkable behavior and find that the S-shaped pores change both the deformation mechanism and the way cracks propagate. More specifically, while in the structures with circular pores large portions of the material are highly stretched, in the case of S-shaped holes most of the structure experiences low values of stress, since the deformation is found to induce rotation of the domains between neighboring holes. As a result, the cracks that are initiated at the stress concentrations along the S-shaped pores get trapped in low stress regions and propagate at a significantly lower rate.

We started by fabricating two stainless steel dog-bone samples patterned with a 5 × 5 square array of circular and S-shaped pores with a center-to-center spacing $L = 10$ mm, as shown in Figs. 1(a) and S1 in *Supplementary Material*. Importantly, both samples are characterized by the same porosity, $\psi = 0.05$. The fatigue life of these structures was determined experimentally by subjecting them to cyclic uniaxial loading under strain-controlled conditions

* Corresponding author at: Harvard John A. Paulson School of Engineering and Applied Sciences, Harvard University, Cambridge, MA, 02138, USA.
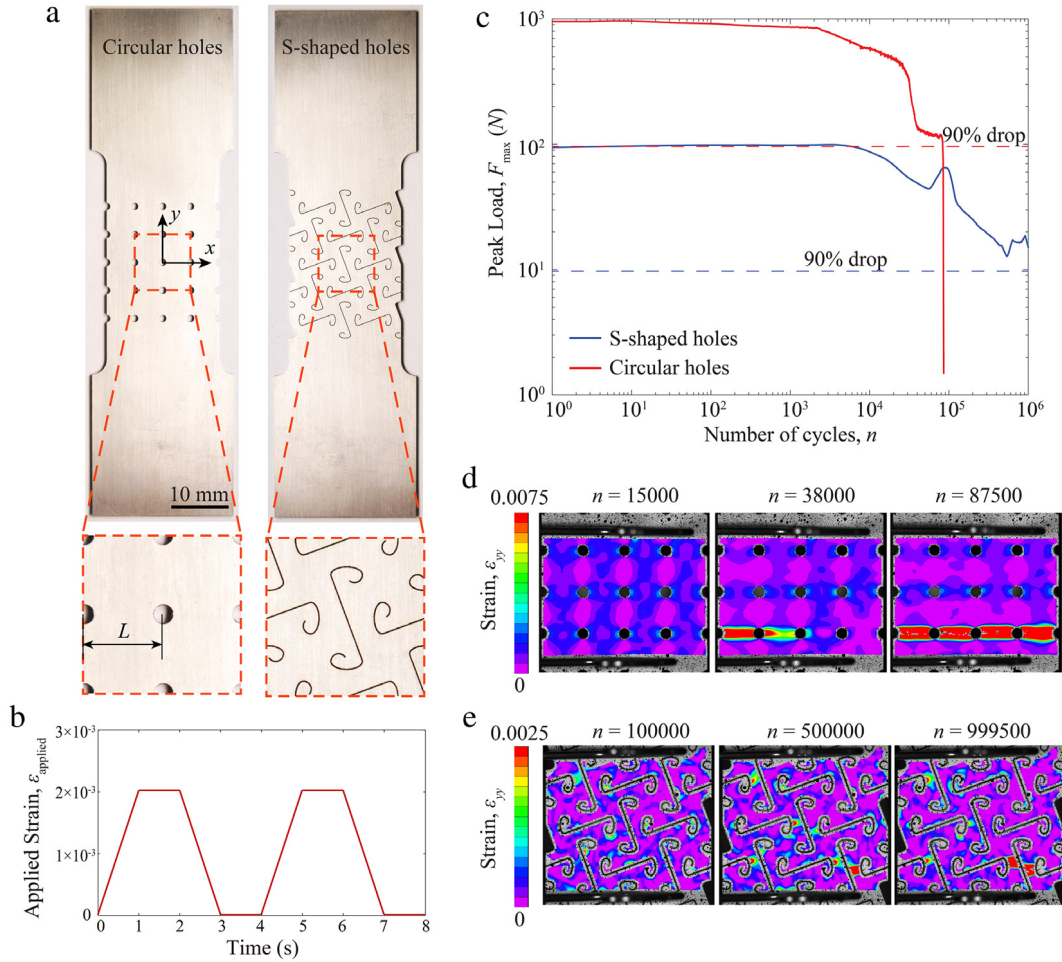*E-mail address:* bertoldi@seas.harvard.edu (K. Bertoldi).

Fig. 1. Experimental results: (a) Dog-bone samples with circular and S-shaped pores. (b) Trapezoidal waveform used in our cyclic tests to control the applied strain. (c) Maximum recorded applied force, F_{max}, versus number of loading cycles, n, for both samples with circular and S-shaped holes. (d)–(e) Contour maps for the longitudinal strain, ε_{yy}, at different values of n for the sample with (d) circular and (e) S-shaped pores.

using an MTS uniaxial testing machine equipped with a 20 kN load cell. All tests were conducted using a trapezoidal waveform with frequency of 0.25 Hz, $\epsilon_{applied}^{max} = 0.002$ and $\epsilon_{applied}^{min} = 0$ (Fig. 1(b)) - see *Supplementary Material* (Appendix A) for more details about the experiments). The specimen failure was defined at the point when a 90% drop in the maximum load (compared to the first cycle) is recorded. Moreover, the evolution of the cracks in the samples versus the number of loading cycles was visualized using digital image correlation (DIC). Finally, we note that these tests, although neglecting the additional stresses induced by the temperature gradients generated by the passage of the cool air through the pores, accurately represent the conditions experienced by gas turbine engine components in each turn on–off cycle.

In Fig. 1(c), we report the peak force in each cycle, F_{max}, versus the number of loading cycles, n, for both samples. We find that the sample with circular holes fails at $n = 85,849$ cycles (red line), while the one with S-shaped holes does not fail up to one million cycles (blue line). Note that this important result is not affected by the chosen definition of specimen failure, since even for different definitions we find that the sample with S-shaped holes is capable of carrying load for many more cycles than the one with circular pores (see Fig. S3 in *Supplementary Material*). The plot also reveals that the peak force for the structure with S-shaped holes is one order of magnitude lower than for that with circular pores. While such loss in stiffness can be very detrimental for load bearing structures, it does not affect the performance of most components of gas turbine engines, since these act as flow

separation between the cold cooling air and the hot flame and are not required to carry any load. More specifically, these parts operate under strain-control conditions, since their major mode of deformation is the thermal expansion imposed by the changes in temperature while the engine is running. Finally, we note that we tested multiple samples and we always found those with S-shaped holes to have significantly enhanced fatigue life, indicating that the effect of holes shape on the fatigue life is significant and robust (see Fig. S4 in *Supplementary Material*).

To get a better understanding of the mechanism resulting in this very different behavior, the evolution of the cracks in the samples versus the number of loading cycles was visualized using digital image correlation (DIC). The contour maps for the longitudinal strain, ε_{yy}, reported in Fig. 1(d) show that for the sample with circular holes a crack is initiated at a hole on the left boundary at $n \approx 20,000$ and then propagates horizontally leading to the complete failure of the sample at $n = 85,849$. In contrast, for the sample with S-shaped pores few cracks that breaks the internal ligaments are found at $n = 500,000$ (see Fig. 1(e)). These cracks, however, do not coalesce so that the sample is still capable of carrying load when the test is stopped after one million cycles.

To fully understand the experimental results, we turned to numerical simulations using the commercial finite element (FE) package ABAQUS/Standard (Simulia, Providence, RI). We first looked at the stress distribution for both structures under monotonic uniaxial tension. To this end, we considered a unit cell with periodic

boundary conditions and performed a static linear analysis assuming a linear elastic response for the material (see *Supplementary Material* (Appendix A) for more details about the simulations). The contour maps for the von Mises stress shown in Fig. 2(a) indicate that the two structures carry the applied deformation very differently. Although in both systems the stress concentrates along the boundaries of the holes, in the structure with S-shaped pores most of the material experiences low values of stress, while in the one with circular pores there are crosses that are highly stretched. This significant difference arises from the fact that for the sample with circular holes the deformation mechanism is stretching, while in the S-shaped hole sample it is mostly rotation of the domains defined by the pores, which also results in a negative Poisson's ratio. Note that identical deformation mechanism has been previously reported for a square array of mutually orthogonal elongated elliptical holes [7,8]. However, by replacing the elliptical holes with S-shaped ones the stress concentrations on the boundary of the pores are significantly reduced (as there are no points with high curvature values) and this postpones crack initiation (see Fig. S8 in *Supplementary Material*).

Importantly, the difference in deformation mechanism significantly affects the crack propagation in these structures. To demonstrate this important point, we started by using the extended finite element method (XFEM) module in ABAQUS/Standard and simulated fracture in a unit cell subjected to monotonic uniaxial tensile loading under plane stress conditions (see *Supplementary Material* (Appendix A) for details). In our numerical analysis we introduced two identical notches of initial length $a_0 = 0.01 L_{min}$ (L_{min} denoting the length of the ligaments separating neighboring holes - Fig. 2(b)) along the boundaries of two pores in the mid-row of each unit cell (at the point characterized by the highest von Mises stress—see Fig. 2(b)). We then monitored the evolution of the crack length as a function of the applied deformation. Note that these are quasistatic analyses and dynamic effects were not taken into account. In Fig. 2(c) we report the evolution of the dimensionless crack length, a/L_{min}, as a function of the applied homogenized strain, $\bar{\varepsilon}_{yy}$, for the unit cells with both circular and S-shaped pores. Interestingly, distinctly different behaviors are observed for these two structures. In the structure with circular pores the cracks start to grow at a relatively early stage (i.e. at $\bar{\varepsilon}_{yy} \approx 3.6 \times 10^{-4}$) and immediately become unstable. As a result, they propagate very quickly through the specimen for increasing values of the applied deformation and the structure fails at $\bar{\varepsilon}_{yy} \approx 1.3 \times 10^{-3}$. By contrast, in the structure with S-shaped pores not only the cracks start to grow for larger values of applied strain (i.e. at $\bar{\varepsilon}_{yy} \approx 6.6 \times 10^{-4}$), but also their growth rate is slower, so that full failure is reached at much larger values of the applied deformation (i.e. at $\bar{\varepsilon}_{yy} \approx 5.4 \times 10^{-3}$).

Next, we investigated how these differences in crack propagation affect the fatigue life of the structures. To this end, we used Paris' law [9], which postulates that the crack growth rate, da/dN, during cyclic loading is

$$\frac{da}{dN} = A \Delta K^m,\qquad(1)$$

where ΔK denotes the variation of the stress intensity factor in each cycle (in our case $\Delta K = K_{max} = K_I|_{\epsilon^{max}_{applied}=0.002}$, since $K_{min} = 0$), and A and m are two constants which depend on material and environmental conditions. For metallic materials, typically $m \in [2, 4]$ and $A \in [10^{-12}, 10^{-6}]$ [10–14]. Finally, we note that Paris' law has been successfully used to predict the fatigue life of structures subjected to cyclic loading under stress-controlled [11,12,15], strain-controlled [16,17], and thermal-controlled [18–21] conditions.

Since Paris' law assumes that the rate of the crack propagation is directly linked to the changes in the stress intensity factor, we performed FE simulations to calculate K_I using the $J-$integral.
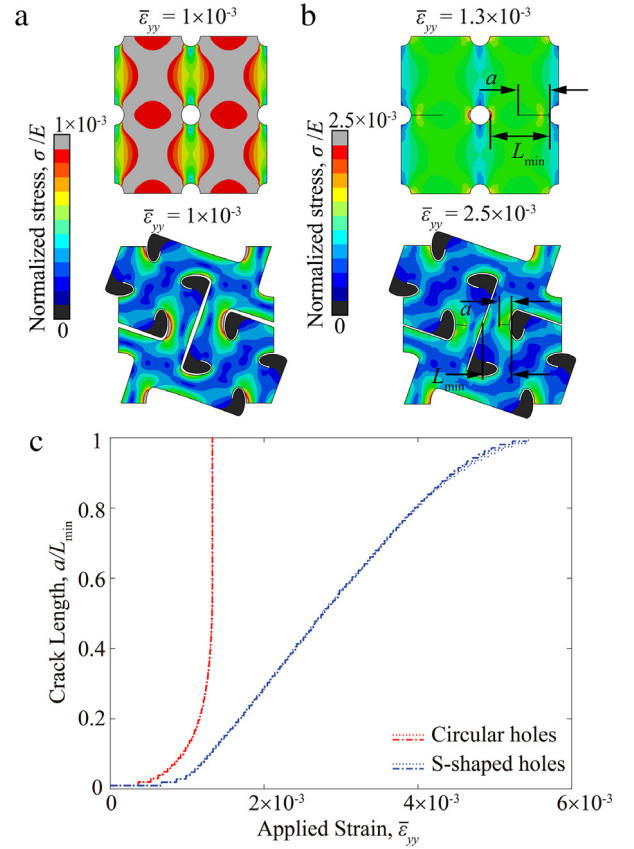

Fig. 2. Numerical analysis: (a) Distribution of von Mises stress (normalized by the bulk material's elastic modulus E) for circular (top) and S-shaped (bottom) holes subjected to monotonic uniaxial tensile loading (in vertical direction) at $\bar{\varepsilon}_{yy} = 1 \times 10^{-3}$. (b) Numerical images showing how fracture propagates in the structure with circular (top) and S-shaped (bottom) holes when subjected to monotonic uniaxial tensile loading. The color indicates the Von Mises stress distributions (normalized by the Young's modulus of the bulk material E). (c) Evolution of the normalized crack length as a function of the applied strain in the structure with circular (red lines) and S-shaped (blue lines) holes. The dashed and dotted lines indicate the length of the cracks propagating from the left and the right sides of the unit cell, respectively. (For interpretation of the references to color in this figure legend, the reader is referred to the web version of this article.)

More specifically, we introduced two line cracks into the FE meshes initiating from the boundary holes in the mid-row of a unit cell (see Fig. 3(a)). Guided by both XFEM simulations and experiments, we assumed that such cracks propagate horizontally and calculated the $J-$integral on a closed contour around the crack tip for different crack lengths, a. Under plane stress assumption and uniaxial loading conditions, the mode I stress intensity factor was then derived from the $J-$integral as $K = \sqrt{EJ}$ [22] (see *Supplementary Material* (Appendix A) for more details). Fig. 3(b) shows the stress intensity factors as a function of a/L_{min} for unit cells with circular and S-shaped pores. The results are fully consistent with those of our XFEM simulations reported in Fig. 2. In fact, we find that, through the whole range of crack lengths considered in simulations, the stress intensity factor in the structure with circular holes is higher than that of the structures with S-shaped pores. According to Eq. (1), this implies that the crack growth rate during cyclic loading is higher for the structure with circular holes, which, therefore, has a shorter fatigue life. Finally, we observe that for the structure with circular holes K increases monotonically with the crack length, whereas for that with S-shaped pores K remains almost constant through the whole range of crack lengths. As a consequence, we expect the crack growth rate da/dN to remain constant for the structure with S-shaped holes and to increase (and eventually to
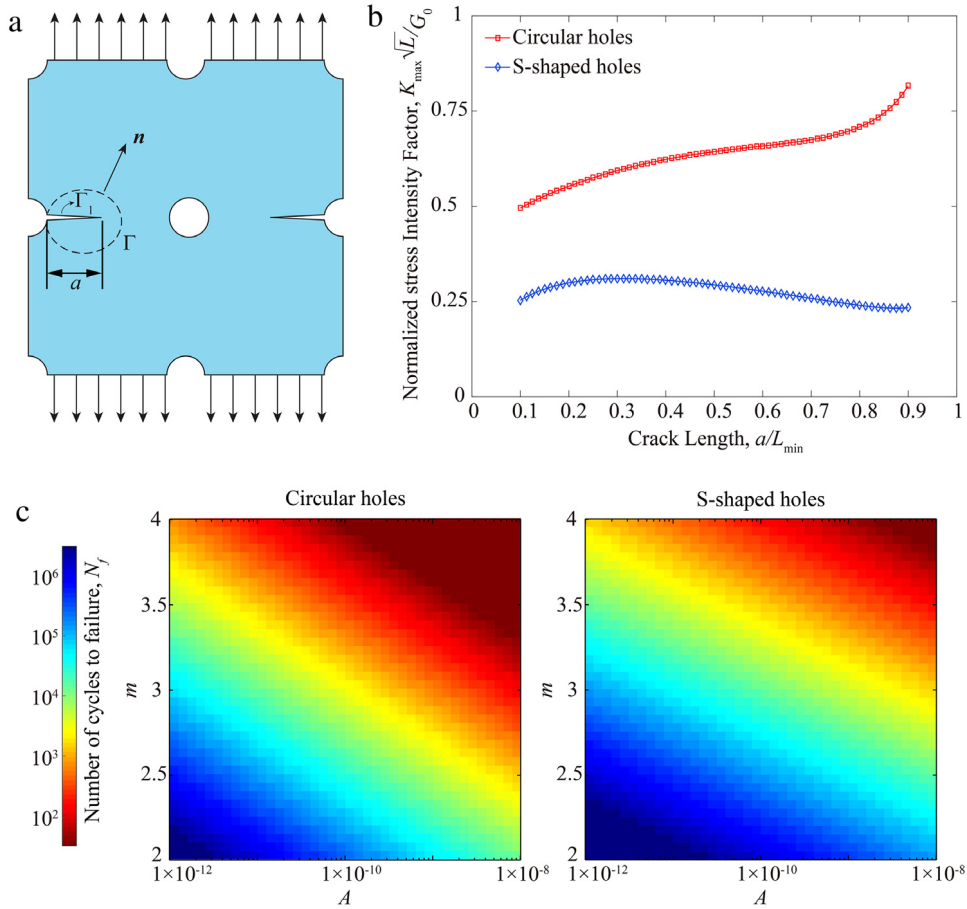
Fig. 3. Numerical analysis: (a) Schematic of the unit cell used to calculate the stress intensity factor, indicating the cracks and the contour path used to calculate K. Unit cells with both circular and S-shaped holes were used in the simulations. (b) Evolution of the stress intensity factor (normalized by $G_0/\sqrt{L}$—where G_0 is the fracture toughness of the bulk material and L is the center-to-center distance between the holes) as a function of the crack length in the structure with circular (red line) and S-shaped (blue line) holes. (c) Contour plot showing the evolution of the number of cycles to failure, N_f, as a function of the Paris law parameters, A and m for the structure with circular (left) and S-shaped (right) holes. (For interpretation of the references to color in this figure legend, the reader is referred to the web version of this article.)

become unstable) as the cracks propagate for the system with circular holes.

Having obtained the stress intensity factor as a function of crack length, the number of cycles to failure, N_f, can be calculated by integrating Eq. (1), yielding

$$N_f = \int_{a_i}^{a_f} \frac{da}{A\,\Delta K^m}. \tag{2}$$

where a_i is the initial crack length at which fatigue crack growth starts and a_f is the critical crack length at which instantaneous fracture occurs. Note that in our calculations we assumed $a_i = 0.1L_{\min}$ and $a_f = 0.9L_{\min}$, since the FE simulations encounter numerical instability for either shorter or longer crack lengths. In Fig. 3(c), we show the evolution of N_f as a function of the material parameters A and m for both circular and S-shaped holes as obtained using Eq. (2) and the numerical prediction of K reported in Fig. 3(b). These contour plots clearly indicate that for any pair of material parameters A and m (i.e. for any combination of material and loading conditions) samples with S-shaped holes are characterized by a longer fatigue life than those with circular pores. Particularly, if we choose $A = 10^{-12}$ and $m = 3.1$ (which have been shown to nicely capture the fatigue life of steel structures [10]) we find that $N_f = 174,419$ and $982,914$ for the structures with circular and S-shaped pores, respectively. These numerical predictions are in good agreement with our experiments.

While in this study we focused on planar samples tested at room temperature, we also expect enhanced fatigue life for porous

sheets with S-shaped holes formed into more complex three-dimensional configurations. To demonstrate this point, we fabricated thin cylindrical shells with radius $r = 36$ mm, height $h = 280$ mm and wall thickness $t = 1$ mm and embedded a square array of S-shaped pores with identical dimensions as those of the planar samples (see Fig. 4(a) - see *Supplementary Material* (Appendix A) for more details). The cylinders were made out of HAYNES 230$^{\circledR}$, a nickel–chromium–tungsten–molybdenum alloy with exceptional high temperature strength [23]. Similar to the planar samples, all fatigue tests were conducted using a trapezoidal waveform with frequency of 0.25 Hz, but $\epsilon_{\text{applied}}^{\max} = 0.004$ and $\epsilon_{\text{applied}}^{\min} = 0$. Moreover, since structures made of HAYNES 230$^{\circledR}$ are typically used in high temperature environments, the experiments are conducted at $T = 600$ and 800 °C. As shown in Fig. 4(b), we find that the cylinders with S-shaped holes are still capable of carrying load and maintaining their structural integrity when the test was stopped after one million cycles. This indicates that we have identified a robust strategy to enhance the fatigue life of porous structures.

In summary, we have shown that the fatigue life of periodic porous structures can be significantly enhanced by carefully designing the shape of the holes. In particular, we introduced a structure with a square array of mutually orthogonal S-shaped pores, for which the applied loading mostly results in rotation of the domains between the neighboring pores. Such rotations lower the stresses in the structure, leading to low stress intensity factors and, consequently, low crack growth rates during cyclic loading.
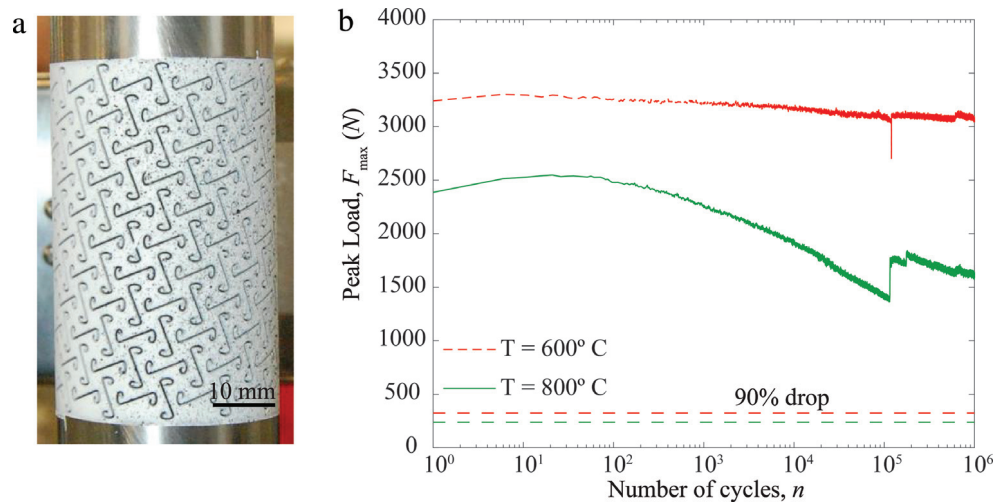
Fig. 4. Experimental results for cylindrical porous structures: (a) Cylindrical sample with S-shaped holes. (b) Maximum recorded applied force, F_{max}, versus number of loading cycles, n, for cylindrical samples with S-shaped holes at $T = 600$ (red line) and $T = 800$ °C (green line). (For interpretation of the references to color in this figure legend, the reader is referred to the web version of this article.)

The proposed structures are also characterized by low porosity, making them suitable candidates for many components of gas turbine engines with cooling requirements. These components will benefit from the proposed design, since it will greatly increase the fatigue life while preserving their low-porosity and, consequently, their cooling performance.

Acknowledgments

Competing Interests The authors declare that they have no competing financial interests.

Appendix A. Supplementary data

Supplementary material related to this article can be found online at http://dx.doi.org/10.1016/j.eml.2017.08.002.

References

[1] H. Saravanmuttoo, G. Rogers, H. Cohen, Gas Turbine Theory, fifth ed., Prentice Hall, 2001.
[2] A.H. Lefebvre, D.R. Balla, Gas Turbine Combustion, third ed., CRC Press, 2010.
[3] K.-D. Lee, K.-Y. Kim, Shape optimization of a fan-shaped hole to enhance film-cooling effectiveness, Int. J. Heat Mass Transfer 53 (15) (2010) 2996–3005.
[4] M. Gritsch, A. Schulz, S. Wittig, Adiabatic wall effectiveness measurements of film-cooling holes with expanded exits, ASME J. Turbomach. 120 (1998) 549–556.
[5] A. Azzi, B.A. Jubran, Numerical modelling of film cooling from converging slot-hole, Heat Mass Transf. 43 (4) (2007) 381–388.
[6] M. Silieti, A.J. Kassab, E. Divo, Film cooling effectiveness from a single scaled-up fan-shaped hole: a cfd simulation of adiabatic and conjugate heat transfer models, ASME Paper No. GT2005-68431 (2005).
[7] J.N. Grima, R. Gatt, Perforated sheets exhibiting negative Poisson's ratios, Adv. Energy Mater. 12 (6) (2010) 460–464.
[8] M. Taylor, et al., Low porosity metallic periodic structures with negative Poisson's ratio, Adv. Mater. 26 (15) (2014) 2365–2370.
[9] P.C. Paris, M.P. Gomez, W.E. Anderson, A rational analytic theory of fatigue, Trend Eng. 13 (1) (1961) 9–14.
[10] H. Park, B. Lee, Effect of specimen thickness on fatigue crack growth rate, Nucl. Eng. Des. 197 (122) (2000) 197–203.
[11] P. Nair, Fatigue crack growth model for part-through flaws in plates and pipes, J. Eng. Mater. Technol. 101 (1) (1979) 53–58.
[12] K. Tanaka, Fatigue crack propagation from a crack inclined to the cyclic tensile axis, Eng. Fract. Mech. 6 (3) (1974) 493–507.
[13] O.G. Bilir, The relationship between the parameters C and n of Paris' law for fatigue crack growth in a SAE 1010 steel, Eng. Fract. Mech. 36 (2) (1990) 361–364.
[14] R. Branco, F. Antunes, J.M. Ferreira, J. Silva, Determination of Paris law constants with a reverse engineering technique, Engineering Failure Analysis 16 (2) (2009) 631–638. Papers presented at the 24th meeting of the Spanish Fracture Group (Burgos, Spain, March 2007).
[15] J. Janson, A continuous damage approach to the fatigue process, Eng. Fract. Mech. 10 (3) (1978) 651–657.
[16] K.R. Lehr, H.W. Liu, Fatigue crack propagation and strain cycling properties, Int. J. Fract. Mech. 5 (1) (1969) 45–55.
[17] F. Lawrence, J. Burk, R. Mattos, Y. Higashida, Estimating the fatigue crack initiation life of welds, in: Fatigue Testing of Weldments, vol. 648, ASTM International, 1978, pp. 134–158.
[18] G. Lloyd, D. Wood, Fatigue crack initiation and propagation as a consequence of thermal striping, Int. J. Press. Vessels Pip. 8 (4) (1980) 255–272.
[19] A. Miller, Crack propagation due to random thermal fluctuations: effect of temporal incoherence, Int. J. Press. Vessels Pip. 8 (1) (1980) 15–24.
[20] T. Shimakawa, et al., Development of the evaluation method for crack propagation due to thermal striping, Nucl. Eng. Des. 138 (3) (1992) 283–296.
[21] J.H. Lau, Thermal fatigue life prediction of flip chip solder joints by fracture mechanics method, Eng. Fract. Mech. 45 (5) (1993) 643–654.
[22] J.R. Rice, A path independent integral and the approximate analysis of strain concentration by notches and cracks, J. Appl. Mech. 35 (1968) 368–375.
[23] D.L. Klarstrom, Oxidation-Resistant Nickel Alloy, US4476091 A, 1982.

Supplementary Material for
On the design of porous structures with enhanced fatigue life

Farhad Javid,[1] Jia Liu,[1] Ahmad Rafsanjani,[1] Megan Schaenzer,[2] Minh Quan Pham,[2] David Backman,[4]

Scott Yandt,[4] Matthew C. Innes, [2] Christopher Booth-Morrison, [2] Miklos Gerendas, [4] Thomas

Scarinci, [4] Ali Shanian, [2] and Katia Bertoldi[1,5*]

[1] *Harvard John A. Paulson School of Engineering and Applied Sciences, Harvard University, Cam-*

bridge, Massachusetts, 02138, USA.

[2] *Siemens power and Gas, 9545 Cote de Liesse, Dorval, Québec, H9P 1A5, Canada.*

[3] *Aerospace Portfolio, National Research Council Canada, 1200 Montreal Road, Building M3,*

Ottawa, Ontario, K1A 0R6, Canada.

[4] *Rolls-Royce Deutschland Ltd. & Co. KG, Dahlewitz, Blankenfelde-Mahlow, Germany.*

[5] *Kavli Institute, Harvard University, Cambridge, Massachusetts, 02138, USA.*

*Corresponding Author. Tel: +1 617 496 3084; E-mail: bertoldi@seas.harvard.edu

S1   Experiments

Fabrication The dog-bone samples were fabricated out of 1 mm thick stainless steel sheets char-

acterized by $E = 193$ GPa and $\nu = 0.33$. A square array of 5×5 holes with a center-to-center

spacing of 10 mm was embedded in their gage section by laser-cutting. Details of the samples

geometry can be found in Fig. S1. The circular holes have radius $R = 0.63$ mm, while the S-
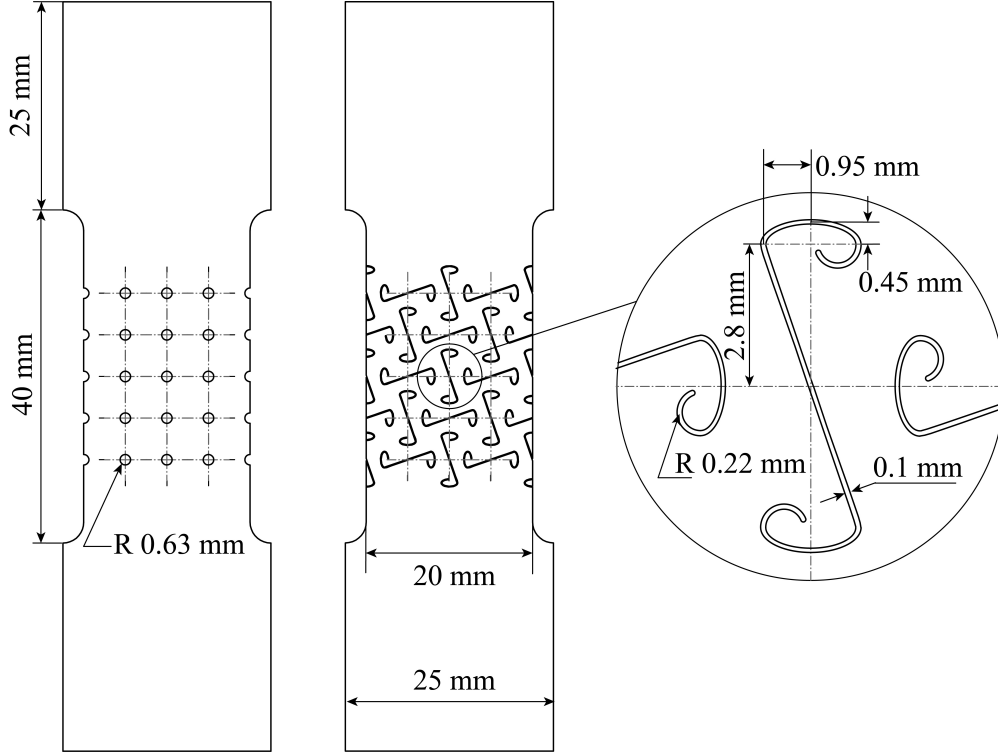
1

Figure S1: Detailed drawings of our dog-bone samples.

shaped pores have a length of 6.6 mm and a width of 2 mm (see zoom-in in Fig. S1 for the details of S-shaped pores). Importantly, both samples are characterized by the same porosity in the gage section, $\psi = 0.05$.

The cylindrical samples were fabricated out of HYNES 230® - a nickel-chromium-tungsten-molybdenum alloy with exceptional high temperature strength. They have radius $r = 36$ mm, height $h = 280$ mm and wall thickness $t = 1$ mm and are patterned with a square array of S-shaped pores with identical dimensions as those of the planar samples. The porosity of the cylinders is $\psi = 0.05$. Note that the cylinders were machined out of a bar and then the pores were embedded by laser drilling.

Testing All experiments were performed in the Aerospace Materials Lab at the National Research Council Canada (ON, Canada) using a MTS uniaxial mechanical tester (MTS Systems Corporation, MN, USA) equipped with a 10 kN load cell. The planar samples were attached to the mechanical tester using two standard hydrophilic grips (see Fig. S2-a). Differently, a special fixture was designed and fabricated to clamp the cylindrical specimens (see Fig. S2-b). Moreover, for the cylindrical structures tested at elevated temperatures, a round furnace was installed around the samples during the tests (see Fig. S2-c) and a thermal survey was conducted to make sure that the desired temperature was reached with acceptable tolerances ($\pm 1\%$.).

The tests were conducted under strain-controlled conditions using a trapezoidal waveform with frequency of 0.25 Hz (see Fig. 1b of the main text). For the planar samples we used $\epsilon_{\text{applied}}^{\max} = 0.002$ and $\epsilon_{\text{applied}}^{\min} = 0$, while for the cylindrical samples we used $\epsilon_{\text{applied}}^{\max} = 0.004$ and $\epsilon_{\text{applied}}^{\min} = 0$. The specimen failure was defined at the point when a 90% drop in the maximum load (compared to the first cycle) was recorded.

The evolution of the cracks in the samples versus the number of loading cycles was visualized using digital image correlation (DIC). During the cyclic tests an AVT Dolphin F-145B camera (Allied Vision Technologies, Stradtroda, Germany) with a resolution of 1392 x 1040 pixels was used to capture the deformation of the samples. Quantitative estimates of the deformation in the gage section of the sample are made using the image correlation software Vic-2D (Correlated Solutions).
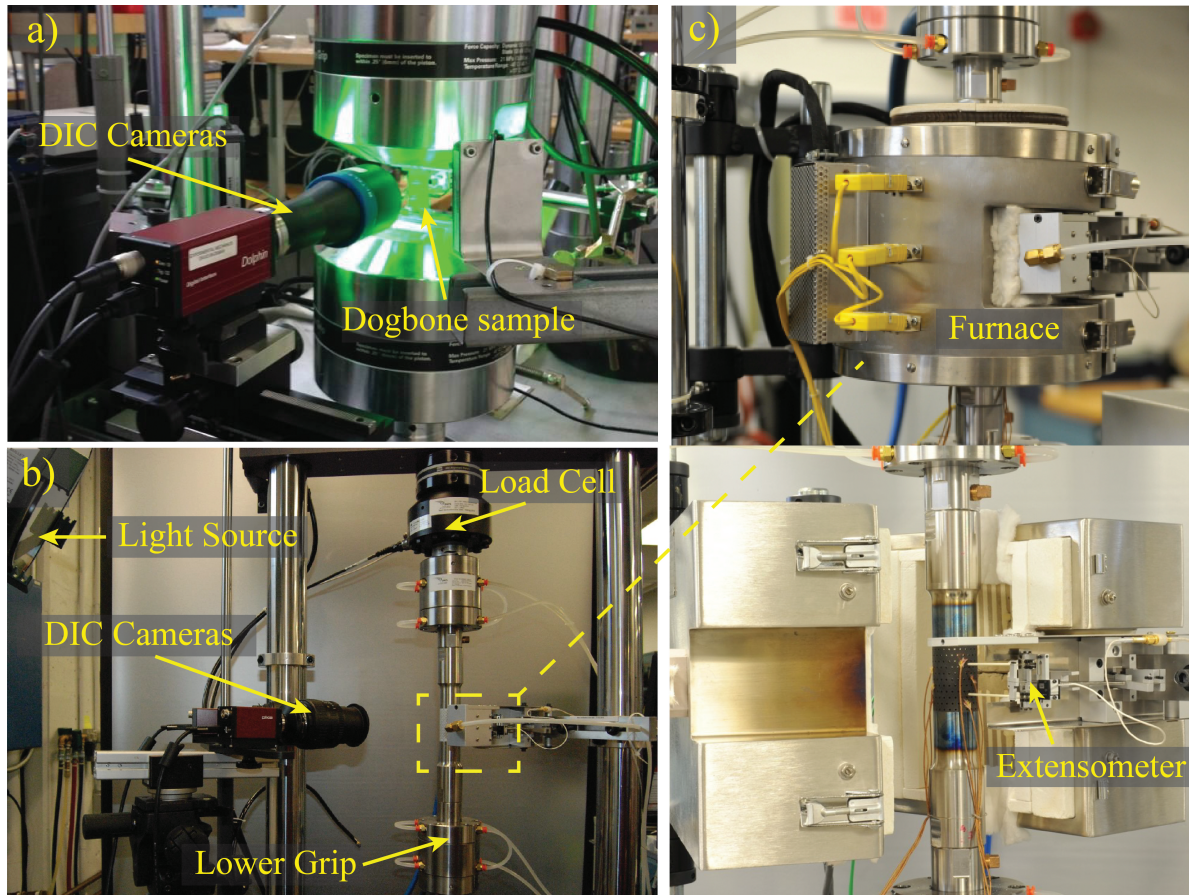
Figure S2: Experimental setup: (a) testing of a planar dog-bone sample; (b) testing of a cylindrical sample at high temperature; (c) a round furnace was installed around the samples during the tests to control the temperature. In the picture on the top we show the closed furnace, while in the bottom one we show it open.

Additional experimental results In the main text, the specimen failure was defined at the point when a 90% drop in the maximum load (compared to the first cycle) is recorded. Such choice is somehow arbitrary and can be changed depending on the application and the safety factors involved in the design. However, our experimental results indicate that, regardless of the chosen definition of specimen failure, the sample with S-shaped holes is always capable of carrying load for many more cycles than the one with circular pores. To highlight this point, in Fig. S3 we report the evolution of the fatigue life ratio between the S-shaped and circular hole samples (defined as $N_f^{\text{S-shaped}}/N_f^{\text{circular}}$, where $N_f^{\text{S-shaped}}$ and N_f^{circular} indicate the number of cycles to failure for the sample with S-shaped and circular holes, respectively) as a function of the specimen failure definition (specified as a percentage of the drop of the maximum load).

In Fig. 1 of the main text we show experimental result for one dog-bone sample with circular holes and one with S-shaped holes. However, we tested several samples and we always found those with S-shape holes to have significantly enhanced fatigue life, indicating that the effect of the holes shape on the fatigue life is significant and robust (see Fig. S4).

High temperature fatigue tests were also conducted on cylindrical structures with circular pores. As shown in Fig. S5, the fatigue life of cylindrical samples with S-shaped holes is significantly higher than samples with circular holes. We should note that the circular holes are patterned in a triangular array on cylindrical structures since such arrangement is more common in turbine engines components.
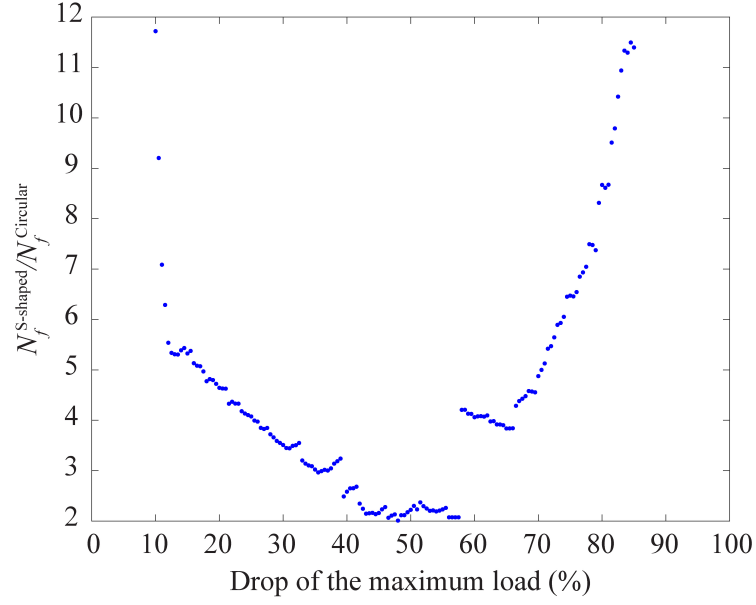
5

Figure S3: Evolution of the fatigue life ratio between the S-shaped and circular hole samples (defined as $N_f^{\text{S-shaped}}/N_f^{\text{circular}}$, where $N_f^{\text{S-shaped}}$ and N_f^{circular} indicate the number of cycles to failure for the sample with S-shaped and circular holes, respectively) as a function of the specimen failure definition (specified as a percentage of the drop of the maximum load).
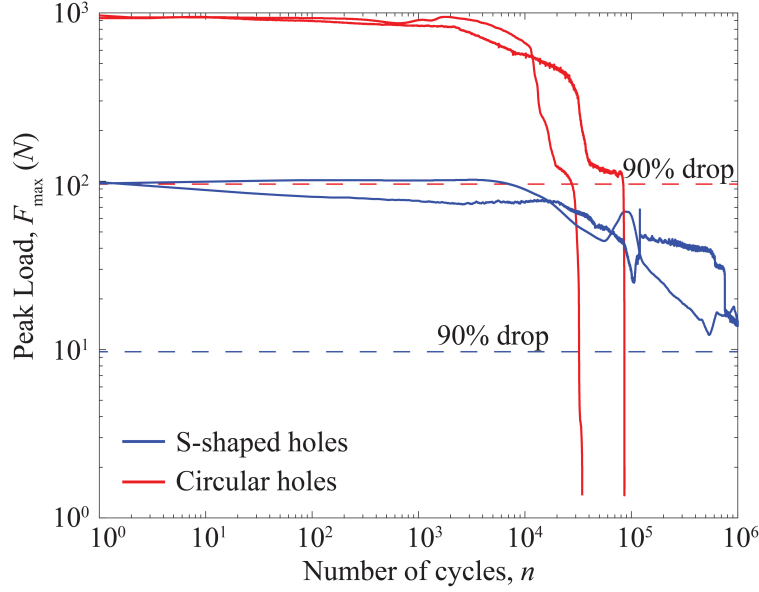
Figure S4: Maximum applied force, F_{max}, versus number of loading cycles, n, for multiple samples with circular and S-shaped holes.

S2 Numerical analysis

For all numerical analysis we used the commercial Finite Element (FE) package ABAQUS (Simulia, Providence, RI). Plane stress 2D elements (ABAQUS element type CPS4 for extended finite element method (XFEM) simulations and CPS8 for static analysis) were used to discretize the models. Moreover, the material response was captured using a linear elastic model with Young's modulus $E = 193$ GPa and Poisson's ratio $\nu = 0.33$. To reduce the computational cost and to ensure the response is not affected by boundary effects, we focused on two-dimensional, infinite periodic structures and considered unit cells with suitable periodic boundary conditions (see Fig. S6) in all simulations. More specifically, we subjected the unit cells to a macroscopic deformation
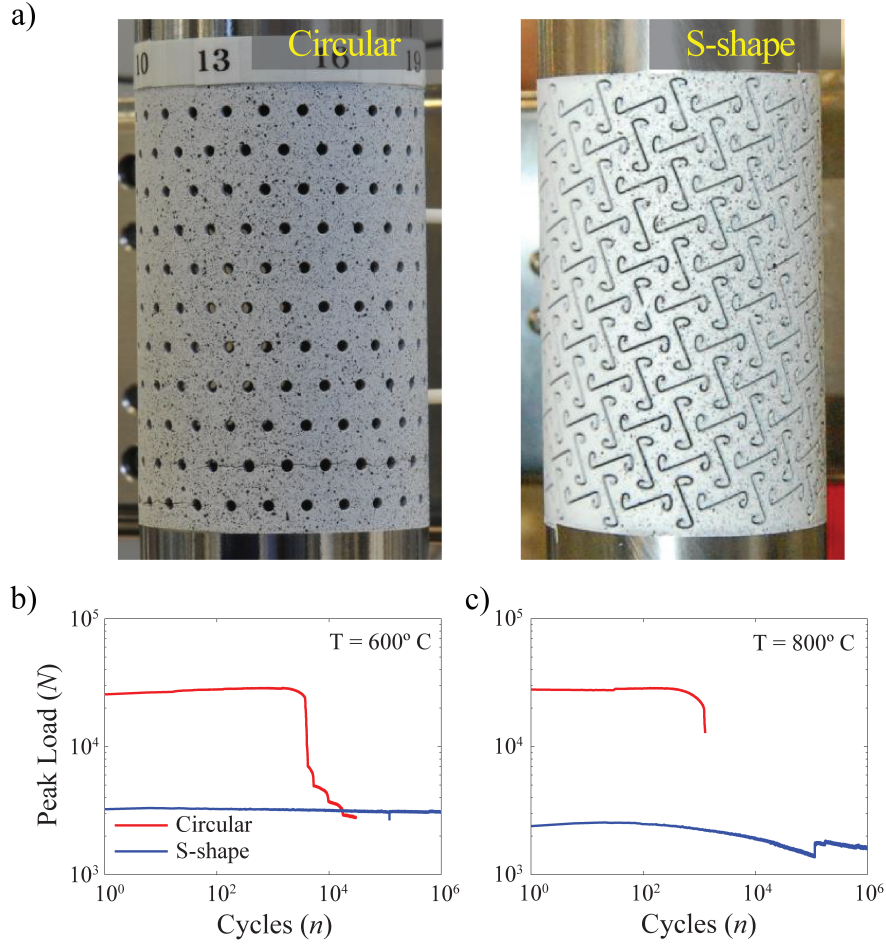
Figure S5: Experimental results for cylindrical structures: (a) samples with circular and S-shaped pores both with 5% porosity (note that the circular holes are arranged on a triangular array). (b)-(c) Maximum recorded applied force, F_{max}, versus number of loading cycles, n, for both pore types at (b) $T = 600°$ and (c) $T = 800°$.
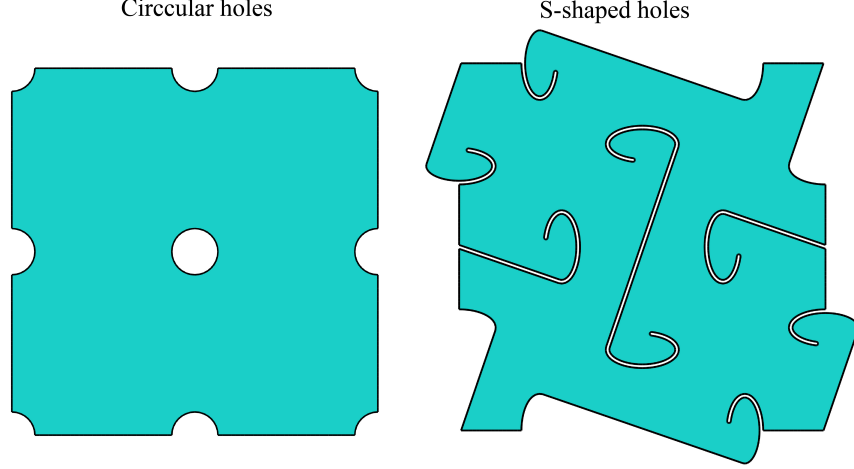
Circcular holes   S-shaped holes

Figure S6: Unit cells used for our numerical simulations.

gradient $\overline{\mathbf{F}}$ by imposing the following periodic boundary conditions on all cell boundaries [1,2]

$$u_\alpha^{A_i} - u_\alpha^{B_i} = (\overline{F}_{\alpha\beta} - \delta_{\alpha\beta})(X_\beta^{A_i} - X_\beta^{B_i}), \quad i = 1,\, 2,\, ...,\, N \tag{S1}$$

where $\delta_{\alpha\beta}$ is the Kronecker delta, $u_\alpha^{A_i}$ and $u_\alpha^{B_i}$ ($\alpha = 1,\, 2$) are displacements of points periodically located on the boundary of the unit cell. Moreover, N denotes the number of pairs of nodes periodically located on the boundary of the unit cell. Note that the components of $\overline{\mathbf{F}}$ can be conveniently prescribed within the finite element framework using a set of virtual nodes. For the case of uniaxial loading in the x_2 direction considered in this study, the macroscopic deformation gradient $\overline{\mathbf{F}}$ is given by

$$\overline{\mathbf{F}} = \lambda_{11}\, \hat{\mathbf{e}}_1 \otimes \hat{\mathbf{e}}_1 + (1 + \varepsilon)\, \hat{\mathbf{e}}_2 \otimes \hat{\mathbf{e}}_2 + \hat{\mathbf{e}}_3 \otimes \hat{\mathbf{e}}_3, \tag{S2}$$

where ε denotes the applied strain in x_2 direction, and λ_{11} is determined from $\sigma_{11} = 0$.

To simulate fracture in a unit cell subjected to monotonic uniaxial tensile, the XFEM module [3–5] in ABAQUS was used. This module allows simulation of initiation and propagation of a dis-

9

crete crack along an arbitrary, solution-dependent path without the requirement of remeshing. The material (stainless steel) was modeled as ductile with a fracture energy of $G_0 = 4 \, \text{J/mm}^2$. Moreover, a traction-separation cohesive behavior, which is suitable for ductile materials, was used to simulate crack initiation and propagation in the material. In particular, we assumed that the damage initiates when the maximum principal stress reaches $\sigma_1 = 250$ MPa and it propagates based on a power-law energy model. Finally, we note that, to facilitate the simulations, two identical notches of initial length $a_0 = 0.01 L_{\text{min}}$ (L_{min} denoting the length of the ligaments separating neighboring holes) were introduced starting from the boundaries of two pores in the mid-row of each unit cell (at the point characterized by the highest von Mises stress - see Fig. 2b of the main text).

To evaluate the fatigue life of the structures, we used Paris' law [6], which postulates that the crack growth rate, da/dN, during cyclic loading is

$$\frac{da}{dN} = A \Delta K^m, \tag{S3}$$

where ΔK denotes the variation of the stress intensity factor in each cycle (in our case $\Delta K = K_{\text{max}} = K_I|_{\epsilon_{\text{applied}}^{\text{max}}=0.002}$, since $K_{\text{min}} = 0$), and A and m are two constants which depend on material and environmental conditions. Since Paris' law assumes that the rate of the crack propagation is directly linked to the changes in the stress intensity factor, we performed static simulations using the STANDARD module in ABAQUS (assuming linear elasticity and small strains) and calculated K_I using the $J-$integral. While in our XFEM analysis we did not prescribe the crack propagation path, for this set of simulations, guided by both our XFEM simulations and experiments, we assumed that the cracks propagate horizontally. Then, we constructed models with two identical horizontal line cracks of length a starting from the boundaries of two pores in the mid-row of each

unit cell (at the point characterized by the highest von Mises stress). More specifically, we built 65 models with different crack lengths

$$a = 0.1\frac{a}{L_{\min}} + j\,0.8\frac{a}{64L_{\min}}, \quad \text{with } j = 0,\,1,\,2,\,....,\,64. \tag{S4}$$

Each model was loaded under uniaxial tension and then the $J-$integral on a closed contour around the crack tip was obtained performing a contour integral analysis in ABAQUS. The mode I stress intensity factor was then derived from the $J-$integral as $K = \sqrt{EJ}$ [7]. Finally, having obtained the stress intensity factor as a function of crack length, the number of cycles to failure, N_f, was calculated by numerically evaluating the integral

$$N_f = \int_{a_i}^{a_f} \frac{da}{A\,\Delta K^m}. \tag{S5}$$

where a_i is the initial crack length at which fatigue crack growth starts and a_f is the critical crack length at which instantaneous fracture occurs. Note that in our calculations we assumed $a_i = 0.1L_{\min}$ and $a_f = 0.9L_{\min}$, since the FE simulations encounter numerical instability for either shorter or longer crack lengths.

Additional numerical results In the main text we focused on porous structures patterned with a square array of circular and S-shaped holes. However, in our numerical analysis we also considered unit cells patterned with a square array of mutually orthogonal elliptical holes. First, we simulated the response under uniaxial monotonic loading of unit cells characterized by the same porosity, $\psi = 0.05$, but patterned with an array of elliptical holes with different aspect ratio, a/b. As shown in Fig. S7, our numerical results indicate that as the aspect ratio of the ellipses increases, the stress pattern in the structure changes. In the unit cell with circular pores, there are crosses that are highly

stretched. In the case of elongated elliptical holes, most of the structure experiences low values of stress and the deformation is found to induce rotation in the domains between holes. We also note that, as for the case of the S-shaped holes, the stress is concentrated around the tips of the ellipses. Such localized stresses are higher for the elliptical holes than for the S-shaped pores. This is because the S-shaped pores are designed to minimize the curvature at stress concentrated points.

Next, we focused on a unit cell with elliptical holes characterized by the same height as the S-shaped pores. Therefore, we chose $a/b = 27$ and used the XFEM module in ABAQUS/Standard to simulate fracture under monotonic uniaxial tensile loading. In Fig. S8 we compare the evolution of the crack length as a function of the applied deformation for unit cells with circular, elliptical and S-shaped holes (note that the results for circular and S-shaped holes are also reported in Fig. 2-c of the main text). The results show that the structures with elliptical and S-shaped holes are characterized by qualitatively similar behaviors and that in both structures the crack propagation is significantly slower than in that with circular holes. In fact, the reduction in the global stress values in elliptical and S-shaped structures traps the cracks after their initiation and hence decreases the crack growth rate. However, the high local stresses around the tips of the elliptical holes result in a higher growth rate.

Finally, we also calculated K_I as a function of the crack length for a unit cell with elliptical holes characterized by $a/b = 27$. Again, the results shown in Fig. S9 indicate that the structures with elliptical and S-shaped holes are characterized by qualitatively similar behaviors. However, the high local stresses around the tips of the elliptical holes result in a higher values for K_I. As
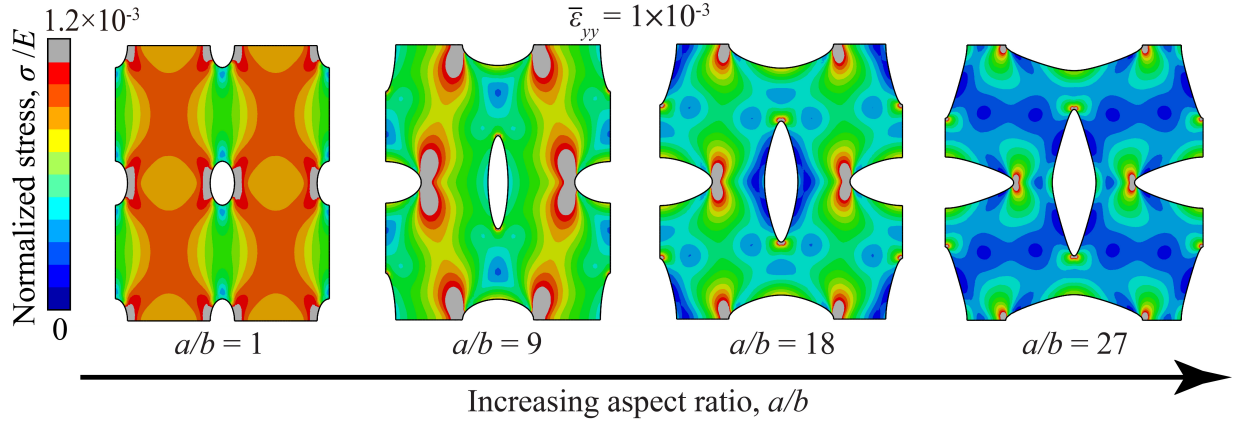
Figure S7: Effect of the hole aspect ratio a/b on the deformation of the structure. Distribution of von Mises stress (normalized by the bulk materials elastic modulus E) for elliptical holes with different values of aspect ratio subjected to monotonic uniaxial tensile loading (in vertical direction) at $\bar{\varepsilon}_{yy} = 1 \times 10^{-3}$.

such, we expect a higher crack growth rate da/dN for the structure with elliptical holes.

1. Danielsson, M., Parks, D. M. & Boyce, M. C. Three-dimensional micromechanical modeling of voided polymeric materials. *Journal of the Mechanics and Physics of Solids* **50**, 351–379 (2002).

2. Bertoldi, K. & Boyce, M. C. Wave propagation and instabilities in monolithic and periodically structured elastomeric materials undergoing large deformations. *Physical Review B* **78** (2008).

3. Manual, A. U. Version 6.12. *Dassault Systémes Simulia Corp., Providence, RI* (2012).

4. Belytschko, T. & Black, T. Elastic crack growth in finite elements with minimal remeshing. *International Journal for Numerical Methods in Engineering* **45**, 601–620 (1999).
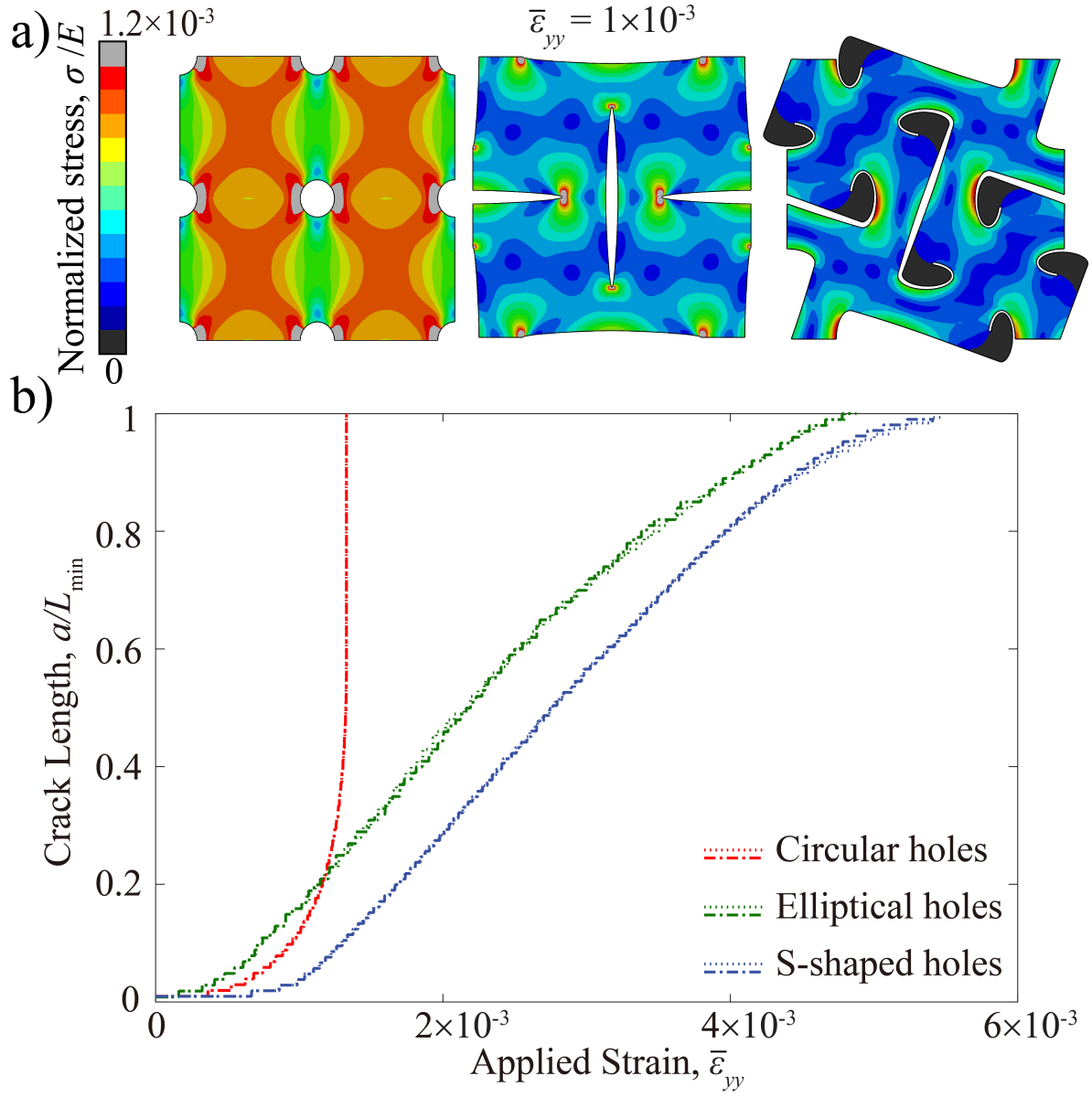
Figure S8: (a) Distribution of von Mises stress (normalized by the bulk material's elastic modulus E) for circular, elliptical and S-shaped holes subjected to monotonic uniaxial tensile loading (in vertical direction) at $\bar{\varepsilon}_{yy} = 1 \times 10^{-3}$. (b) Evolution of the normalized crack length as a function of the applied strain in the structure with circular (red lines), elliptical (green lines) and S-shaped (blue lines) holes. The dashed and dotted lines indicate the length of the cracks propagating from the left and the right sides of the unit cell, respectively.
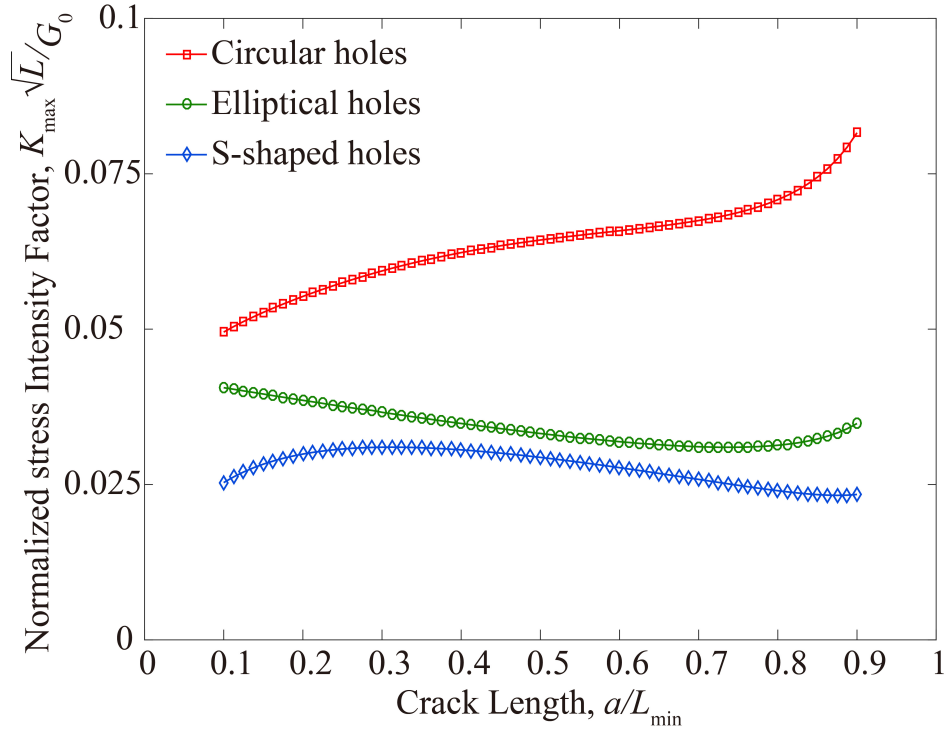
Figure S9: Evolution of the stress intensity factor (normalized by $G_0/\sqrt{L}$ (where G_0 is the fracture toughness of the bulk material and L is the center-to-center distance between the holes) as a function of the crack length in the structure with circular (red line), elliptical (green line) and S-shaped (blue line) holes.

5. Sukumar, N. & Prvost, J.-H. Modeling quasi-static crack growth with the extended finite element method part i: Computer implementation. *International Journal of Solids and Structures* **40**, 7513 – 7537 (2003).

6. Paris, P. C., Gomez, M. P. & Anderson, W. E. A rational analytic theory of fatigue. *The trend in engineering* **13**, 9–14 (1961).

7. Rice, J. R. A path independent integral and the approximate analysis of strain concentration by notches and cracks. *Journal of Applied Mechanics* **35**, 368–375 (1968).